Impact of high-order interactions on the fundamental dynamics of four-wave mixing

Anastasiia Sheveleva,[1,*] Pierre Colman [1], John M. Dudley [2] and Christophe Finot [1]

[1]*Laboratoire Interdisciplinaire Carnot de Bourgogne, UMR 6303 CNRS, Université de Bourgogne, Dijon 21000, France*

[2]*Institut FEMTO-ST, CNRS 6174 UMR, Université de Franche-Comté, 25000 Besançon, France*

We extend the truncated three-wave theory used to describe degenerate four-wave mixing in optical fibers to take into account the impact of higher-order harmonic sidebands. Using second-order perturbation theory combined with adiabatic elimination, our extended theory preserves the initial framework of the three-wave description. This allows the subsequent discussion of the origin of the nonpreservation of the Fermi-Pasta-Ulam-Tsingou recurrence that is observed in optical fibers. Our analytical results are supported by numerical simulations and experimental observations.

I. INTRODUCTION

The wave dynamics in a dispersive medium subject to an intensity-dependent refractive index is governed by the non-linear Schrödinger equation (NLSE) [1], which is one of the seminal equations in science. It can be applied to numerous different domains, including hydrodynamics, plasma physics, Bose-Einstein condensates, and the propagation of light in optical fibers [2–4].

One of the most important NLSE processes at the core of numerous fundamental discoveries and practical applications is the modulation instability (MI) [5,6] which manifests in a form of spontaneous or seeded amplification of spectral harmonics [7,8]. The initial stage of the MI can be described in terms of four-wave mixing (FWM) events which change the relative phase and redistribute the optical energy among the individual harmonics [9–11]. The understanding of this fundamental process improved after the development of an analytical truncated three-wave model operating in terms of conjugate variables [12–14]. It revealed the existence of different types of energy-conversion processes depending on the optical phase, as well as recursive dynamics patterns referring to the celebrated Fermi-Pasta-Ulam-Tsingou (FPUT) recurrence [15,16]. Indeed, the nonlinear Schrödinger equation that governs the evolution of a frequency comb composed of discrete optical lines in an optical fiber has the same form as the seminal FPUT equation after canonical transformation [17]. Considering the fundamental importance of modulation instability in nonlinear optics, this analogy has attracted strong interest from the fiber-optics community. Owing to the difficulty of investigating and controlling large systems, experimental works have focused on cases dealing with only a few lines rather than the seminal 32 lines of the numerical FPUT model. Still, optical breathers exhibiting a complex recurrence dynamics were observed. It is worth noting that the FPUT recurrence in fiber optics can be demonstrated only

under specific conditions excluding the impact of linear losses, third-order chromatic dispersion, and noise which would ultimately lead to recurrence breaking [18–21]. Nevertheless, there have been successful experimental demonstrations and studies of FPUT dynamics; for instance, in [22–24] the authors observed quasirecurrence over several cycles, while in other cases, the breathing solutions were demonstrated [8,25–27].

That said, real optical systems deviate from the ideal NLSE paradigm because they are subject to perturbations, such as the presence of higher-order harmonics and propagation loss. As a result, they undergo qualitative changes in their dynamics [20,28]. In particular, it was demonstrated that linear losses in optical fibers can cause dissipation, which results in the breaking of the recurrence cycles. More recently, we developed an experimental setup allowing us to limit wave interactions to only three spectral lines, but with complete control of both the optical amplitude and phase, which is determinant to demonstrate experimentally the fundamental FWM process [29] and the minimal example of FPUT recurrence in optical fibers. In that work we successfully reproduced typical features of the truncated model under various initial conditions. However, we also observed certain deviations from the ideal dynamics in the form of slight disturbances in the FPUT-like cycles over long propagation lengths. Moreover, the characteristic invariants of the underlying Hamiltonian dynamics are not preserved either. In [30], we revealed that changes in the comb asymmetry originate from the impact of residual second-order sidebands. Following experimental demonstrations evidencing systematic deviation from the ideal three-wave mixing, even in the situation where extra sidebands and any other deviation from the nominal NLSE system are negligible, we now would like to discuss more globally the origins of the disturbance that appears in any truncated system and of the nonconservation of its associated Hamiltonian.

We are not aware of other works that extend the truncated FWM equations to include higher-order interactions while preserving the structure of the model. When discussing analytical models governing such systems, most of the studies focus

---

*Contact author: anastasiia.sheveleva@outlook.com

on per-harmonic differential equations without connections to Hamiltonian dynamics [9–11]. In [13], the same authors who developed the truncated model for FWM with a degenerate pump extended it to the nondegenerate case. However, this study was still limited to describing the interaction of only four spectral lines.

In this article, we improve the accuracy of the model while still retaining the nominal truncated three-wave description of the dynamics. It now encompasses the effects of higher-order sidebands. It serves, then, as an aid to discussing the onset of cascaded four-wave mixing and how the underlying Hamiltonian dynamics is actually perturbed by the presence of additional nonlinear mixing processes, which were not considered in the initial truncated system.

II. FUNDAMENTAL FOUR-WAVE MIXING DYNAMICS AND ITS LIMITS

A. Truncated FWM model

Nonlinear propagation along an optical fiber obeys the focusing nonlinear Schrödinger equation, which reads, in its normalized form,

$$i\frac{\partial A(\xi,\tau)}{\partial \xi} + \frac{1}{2}\frac{\partial^2 A(\xi,\tau)}{\partial \tau^2} + |A(\xi,\tau)|^2 A(\xi,\tau) = 0, \quad (1)$$

where $A(\xi,\tau) = \psi(z,t)/\sqrt{P_0}$ is the optical field normalized to the average power P_0, $\xi = z/L_{NL}$ is the normalized propagation distance, $\tau = t/\sqrt{|\beta_2|L_{NL}}$ is the normalized temporal axis, and $L_{NL} = (\gamma P_0)^{-1}$ is the nonlinear length. γ and β_2 denote the nonlinear Kerr parameter and the second-order dispersion, respectively.

We restrict Eq. (1) to only three spectral components which are modeled by ideal delta functions and are equally spaced by the normalized pulsation $\omega_m = 2\pi f_m \sqrt{|\beta_2|/\gamma P_0}$. Then we can substitute the ansatz $A(\xi,\tau) = A_0(\xi) + A_{-1}(\xi)\exp(i\omega_m\tau) + A_1(\xi)\exp(-i\omega_m\tau)$ (with the carrier frequency omitted) into the NLSE. Following the guidelines in [12], the dynamics is now described by one coupled equation for each spectral harmonic. The phase and the amplitude of each wave can be separated, $A_i(\xi) = a_i(\xi)\exp[i\varphi_i(\xi)]$, resulting in a final set of six differential equations. Using the canonical transformation $\eta(\xi) = |a_0(\xi)|^2/\sum_{i=-1}^{1}|a_i(\xi)|^2$ as the relative spectral amplitude and $\phi(\xi) = \varphi_{-1}(\xi) + \varphi_1(\xi) - 2\varphi_0(\xi)$ as the relative spectral phase, the set of coupled equations can be further simplified into the evolution of a one-dimensional nonlinear Hamiltonian oscillator [12],

$$\frac{d\eta}{d\xi} = \frac{\partial H(\eta,\phi)}{\partial \phi} = -2\eta(1-\eta)\sin\phi, \quad (2a)$$

$$\frac{d\phi}{d\xi} = -\frac{\partial H(\eta,\phi)}{\partial \eta} = (\kappa - 1) + 3\eta - (2 - 4\eta)\cos\phi. \quad (2b)$$

η and ϕ form a set of conjugate variables, so $H(\eta,\phi)$ represents the Hamiltonian of the system:

$$H(\eta,\phi) = 2\eta(1-\eta)\cos\phi - (\kappa - 1)\eta - \frac{3}{2}\eta^2. \quad (3)$$

It is quite remarkable that a truncated three-comb-line evolution, corresponding to the minimal configuration to observe FWM and MI, can be reduced to a one-dimensional nonlinear
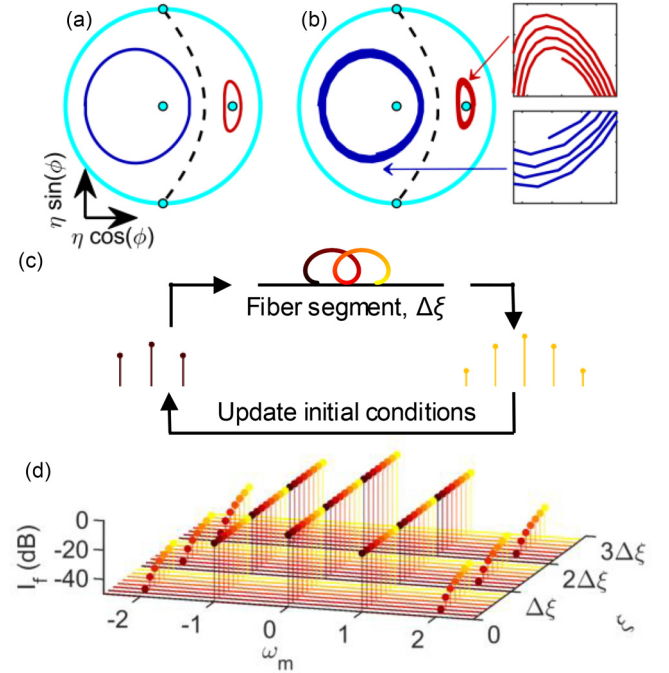

FIG. 1. (a) Fundamental FWM dynamics according to Eq. (2) over $\xi = 16$ at $\kappa = -2$, $\eta_0 = 0.80$, and $\phi_0 = 0$ and π (red and blue lines, respectively). The black dashed line indicates the position of the separatrix. Cyan dots indicate the position of the constant solutions of Eq. (2). Only the solutions located at $\eta = 0$ and $(\eta = (3 - \kappa)/7, \phi = 0)$ are stable. Note that because of the polar representation, the solution $\eta = 1$ appears as the unit circle. (b) The FWM dynamics in a numerical simulation replicating the experiment demonstrates the spiraling dynamics [the simulation parameters are the same as in (a)]. (c) Experimental concept in which the input conditions are continuously updated after three waves propagate in a small segment of fiber [29]. (d) Simulated changes in spectral amplitudes during a few consecutive iterations.

oscillator. Since the FWM process depends strongly on the phase-matching conditions between the spectral lines [31], the dynamics is controlled by a single normalized nonlinear mismatch parameter, $\kappa = \text{sgn}(\beta_2)(2\pi f_m)^2|\beta_2|/\gamma P_0$. Maximal MI gain is obtained for $\kappa = -2$ (it occurs for a reduced comb spacing of $\omega_m = \sqrt{2}$). Experimentally, the value of κ can be easily tuned either by changing the frequency spacing f_m between the input comb lines or by varying the total optical power P_0. Note that in this paper we consider the sidebands at $\pm\omega_m$ to be symmetric, e.g., to have equal spectral amplitudes and relative phases, which leads to simplified forms of Eqs. (2) and (3) [12].

Using the description of the system in terms of its reduced variables (η,ϕ), one can display the dynamics on the phase-space plane [20,32]. Here, we use a polar coordinate representation, $(\eta\cos\phi, \eta\sin\phi)$; a few typical trajectories are displayed in Fig. 1(a). This representation allows to conveniently distinguish the dynamics with bounded and unbounded phases (red and blue lines, respectively). Four stationary solutions exist, as indicated by cyan circles. The solution located at $\eta = 1$ is unstable. One stationary and stable solution exists for each class of orbits. The two classes

of trajectories are divided by the fourth unstable solution, called the separatrix, that connects the points ($\eta = 1$, $\phi = \pm \cos^{-1}[-(\kappa + 2)/2]$). In the present paper we often refer to these two types of dynamics as solutions belonging to the right and left sides of the separatrix.

Such a system, where the dynamics is strictly limited to three spectral lines, is considered to be ideal or fundamental four-wave mixing (FWM) in its degenerate case. Variations in amplitude and phase follow closed trajectories that are completely defined by κ and the Hamiltonian energy (or, equivalently, the initial conditions) [33]. The Hamiltonian (namely, energy) value which is preserved during propagation represents the conservation of the time-averaged energy of the field. The two stable stationary solutions, which represent waves propagating with no changes in either the relative phase or the relative amplitude, are located at the extreme positions of the Hamiltonian ($\frac{\partial H(\eta, \phi)}{\partial \phi} = 0$, $\frac{\partial H(\eta, \phi)}{\partial \eta} = 0$) [12].

B. Principle of the experimental approach

Experimental demonstration of the fundamental FWM in optical fibers is a rather challenging task. The effects of propagation losses and the generation of higher-order sidebands that naturally occur in the fiber cause a deviation from the ideal model and break the FPUT recurrence [30,34]. This is a fundamental difference that exists between the nominal FPUT model and the nonlinear evolution of an optical frequency comb obeying the NLSE equation. The number of oscillators in the numerical FPUT model is fixed, while new comb lines are always spontaneously created in an optical fiber, unless specific mitigation measures are taken. In our previous works, we constructed an experimental setup aiming to demonstrate fundamental FWM [29]. The main idea of the experimental approach [displayed in Fig. 1(c)] was to tailor the input signal's parameters (η_i, ϕ_i) with a programmable spectral filter and then propagate it in a small segment of fiber $\Delta\xi$. After measuring the output parameters (η_{i+1}, ϕ_{i+1}), we update the input conditions and iterate this process in a loop. This allows us to reproduce the ideal FWM dynamics over long propagation distances: over 50 km, or $\xi = 12$, at $\kappa = -2$ in a 500-m fiber with $\gamma = 1.7$ (W km)$^{-1}$ and $\beta_2 = -8$ ps^2 km^{-1}.

This method allows us to exclude the impact of propagation losses and limits generation of the higher-order sidebands at $\pm p\omega_m$ ($p \geqslant 2$). After each iteration, we update the parameters of the three central harmonics ($-\omega_m$, 0, ω_m), while others are filtered out in the recycling process. Nevertheless, we cannot completely exclude their generation as light propagates in the fiber, and we observe the occurrence of second-order sidebands with a level below 1% of the total spectral intensity. Figure 1(d) showcases the gradual growth of spectral lines at $\pm 2\omega_m$ which are filtered after each iteration of $\Delta\xi$, so the process starts anew at updated values of (η_{i+1}, ϕ_{i+1}).

The impact of the second-order harmonics is not pronounced over short propagation distances (<50 km), and FPUT-like recurrences are observed. However, the accumulation of these small perturbations results in the case of longer propagation length in the deviation from the closed orbits.

This behavior is presented in Fig. 1(b), where signals with the same initial conditions as in Fig. 1(a) propagate over $\xi = 16$ in the numerical simulation, emulating experimental conditions (segmented propagation according to the NLSE with recycling of the three-wave parameters after each $\Delta\xi = 0.128$). We observe that the trajectories indeed do not follow the closed orbits anymore and begin to spiral inwards. Similar behavior has been observed experimentally: Trajectories stay within the same dynamics type (with bounded or unbounded phase), but the FPUT recurrence is not perfectly preserved.

Considering that this systematic trend is slow and reveals itself fully only during long propagation, we ruled out any experimental artifact by setting up a numerical analog of the experiment. In brief, we solve numerically the NLSE equation (1) over a distance $\Delta\xi$ for an optical input field composed of three Dirac-like lines, corresponding to the input state (η_{in}, ϕ_{in}). The NLSE is solved using the split-step method, and the frequency grid is chosen to match a subharmonic of the comb spacing in order to avoid any spectral leakage (especially scalloping loss) when performing the successive Fourier transforms. The output state (η_{out}, ϕ_{out}) is extracted from the output optical field and serves as the input conditions for the next NLSE propagation of segment $\Delta\xi$. Considering that the numerical analog and the experimental evidence are consistent, we will use the former for comparison with theoretical models because it provides a larger and more accurate (i.e., artifact-free) dataset.

III. DEVELOPMENT OF A MODIFIED FWM MODEL

A. Impact of the second-order harmonics

As soon as their existence is permitted, second-order harmonics are created and interact with the three central lines. This corresponds to the opening of new mixing (i.e., nonlinear scattering) paths for the photons. By adding these new mixing possibilities to Eq. (2), the observed deviation from the ideal dynamics must then be reproduced.

This would, however, complexify the theoretical model from two coupled equations to five. That said, the amplitude of the second-order harmonics remains small, and they impact the dynamics only after a large propagation distance. Therefore, the extended system can be understood as a Hamiltonian system (the three central lines) with weak interaction with a coherent but dissipative reservoir (the second-order harmonics). The equations for second-order harmonics can be solved in terms of the reduced variables (η, ϕ), and their effects can then be incorporated adiabatically in the nominal system of Eq. (2). In contrast to previous derivations of FWM in which the increase in accuracy was made at the cost of simplicity (one more equation per extra sideband) [9–11,35], the present demonstration retains the original simplicity of the system.

In detail, to formulate the modified model, we take an approach similar to that in our previous work in which we discussed the nonconservation of the asymmetry invariant in the experimental dynamics [30]. First, the second-order sidebands are growing from noise, and at low values of κ (< -1), the modulation-instability-gain bandwidth does not include them. As a result they are neither amplified nor generated efficiently. In this context, we can therefore consider only stimulated processes (see Fig. 6 in the Appendix) and neglect spontaneous FWM. The mathematical derivation and the resulting final

system of coupled equations for the waves' amplitudes and phases are described in the Appendix.

For a segment $\Delta\xi$ small enough with respect to the characteristic evolution length of the unperturbed FPUT recurrence (defined as the length required to observe one recurrence cycle), the equations governing the evolution of the extra sidebands [Eq. (A1)] can be integrated to result in the following amplitude for the second-order sidebands:

$$a_{\pm 2} = \frac{\Delta\xi}{4}\sqrt{\eta}(1-\eta)[\sin(\varphi_{\pm 2} - \phi) + 2\sin\varphi_{\pm 2}]. \quad (4)$$

Note that the transfer of energy to the ± 2 sidebands is a phase-dependent process. The maximal growth of the $a_{\pm 2}$ sidebands will actually happen if all the photons are scattered into them constructively with the same phase, resulting in a net coherent accumulation of energy. When (η, ϕ) vary over a small $\Delta\xi$, this situation corresponds mathematically to $\frac{d\varphi_{\pm 2}}{d\xi} = 0$, which thus gives

$$\varphi_{\pm 2} = -\tan^{-1}\left(\frac{2+\cos\phi}{\sin\phi}\right) + \pi M. \quad (5)$$

$M = 1$ if $\sin\phi > 0$, and $M = 0$ otherwise.

In the case in which spectral lines are amplified by noise in an undepleted pump approximation and $\phi = 0$, we reconstruct the relative phase of $\pm\pi/2$ from Eq. (5) [36–38]. In other cases, this expression gives the correct approximation of the second-order sidebands' phase, which was verified in our numerical simulation of the iterated NLSE propagation.

B. Complete modified model

After solving the equations in a the undepleted pump approximation, the second-order harmonics can be expressed only as a function of the reduced variables. Equation (2) can therefore be complemented by a corrective term involving only the latter; hence, we obtain

$$\frac{d\eta}{d\xi} = -2\eta(1-\eta)\sin\phi$$
$$+ \frac{1}{2}\Delta\xi\eta(1-\eta)^2[(1+\eta)\sin^2(\varphi_{\pm 2} - \phi)$$
$$+ 4\eta\sin\varphi_{\pm 2}\sin(\varphi_{\pm 2} - \phi) + 4(\eta - 1)\sin^2\varphi_{\pm 2}], \quad (6a)$$

$$\frac{d\phi}{d\xi} = (\kappa - 1) + 3\eta - 2(1 - 2\eta)\cos\phi$$
$$+ \frac{1}{4}\Delta\xi(1-\eta)[\sin(\varphi_{\pm 2} - \phi) + 2\sin\varphi_{\pm 2}]$$
$$\times[4(3\eta - 1)\cos\varphi_{\pm 2} + (5\eta - 1)\cos(\varphi_{\pm 2} - \phi)]. \quad (6b)$$

Here, the first part of the equation is responsible for the fundamental FWM processes [Eq. (2)], which are also preserved in the modified model. The second part appears only due to the existence of additional stimulated photon-mixing processes which lead to the energy exchange with the second-order harmonics with the phase $\varphi_{\pm 2}$ given by Eq. (5). Such a simplification of the model is possible only by assuming perturbative adiabatic growth of the ± 2 spectral lines.

Note that Eq. (6) is valid for only short segment lengths $\Delta\xi$, as discussed previously. If $\Delta\xi$ is large, the assumptions about small growth and constant phase are no longer valid,
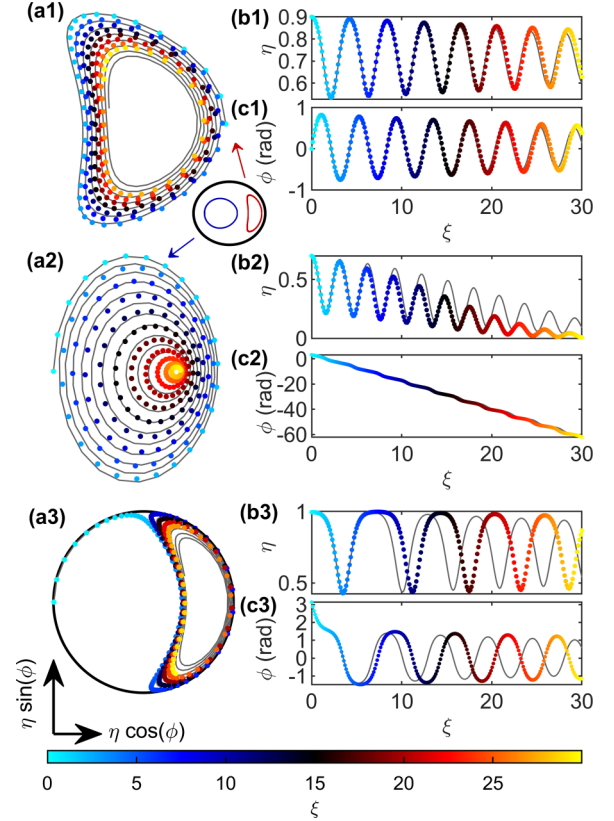

FIG. 2. FWM dynamics according to numerical simulations (solid lines) and the modified model Eq. (6) (colored points). The inset shows the positions of each trajectory on the phase-space map and solutions according to the ideal truncated model. Input parameters are (a1)–(c1) $\eta_0 = 0.90$ and $\phi_0 = 0$, (a2)–(c2) $\eta_0 = 0.70$ and $\phi_0 = \pi$, and (a3)–(c3) $\eta_0 = 0.995$ and $\phi_0 = \pi$ at $\kappa = -2$ and $\Delta\xi = 0.128$. (a)–(c) display evolution on the phase-space plane, changes in the relative amplitude η, and phase ϕ with propagation distance, respectively.

which would lead to discrepancies between the model and the segmented NLSE propagation.

To verify our model, we numerically simulate the experimental dynamics by using segmented propagation of the NLSE. We choose a propagation length of $\xi = 30$ (216 segments of $\Delta\xi = 0.128$), which allows us to observe a significant spiraling and hence benchmark the solutions of Eq. (6). The results are presented in Fig. 2 for initial conditions $\eta_0 = 0.90$ and $\phi_0 = 0$ [Figs. 2(a1)–2(c1)], $\eta_0 = 0.70$ and $\phi_0 = \pi$ [Figs. 2(a2)–2(c2)], and $\eta_0 = 0.995$ and $\phi_0 = \pi$ [Figs. 2(a3)–2(c3)] at $\kappa = -2$, which implies the maximum modulation instability gain for the ± 1 sidebands.

We note very good agreement of the numerical results and our modified model, especially in the early stages of propagation. With further propagation, the dynamics starts to deviate from numerical predictions, which can be ascribed to (1) the accumulation of inaccuracies that arise from analytical assumptions regarding $\varphi_{\pm 2}$ and the processes included and (2) the fact that η tends to decrease with distance, which means that the sidebands are becoming stronger and starting to act as two pumps symmetrically located with respect to the

central frequency, which ultimately leads to the development of additional photon-exchange processes that are not included in our model (this would correspond to the growth of third-order harmonics and could be, to some extent, related to the discussion in [13]). The accumulation of these effects can ultimately break the recurrence when the trajectory passes near the unstable solution, which leads to the separatrix crossing depicted in Figs. 2(a3)–2(c3).

IV. STATISTICAL PROPERTIES AND DISSIPATION OF HAMILTONIAN DYNAMICS

As demonstrated in the previous section, the system follows spiraling trajectories gradually, away from the initial closed orbits. This behavior can be explained by the fact that global attractors may exist on the phase-space plane and that the dynamics is impaired by dissipation. Therefore, the next question is to investigate the statistical properties of the dynamics and redefine the Hamiltonian.

A. Statistical estimation of attraction regions

To define the attraction regions, we both run a numerical simulation and solve the extended theoretical model over a very long propagation distance, $\xi = 255$, for various initial conditions on a grid covering the full phase space. We consider 112 trajectories, which allows us to make conclusions about the number and loci of the attractors and their respective basins of attraction characterized by the density parameter. It is defined by counting, for each phase-space map's grid point, how many time each trajectory passes through it. Since one of the parameters controling the dynamics in our system is the segment length, we repeat the simulation for $\Delta\xi = 0.064, 0.128, 0.192, 0.255$.

First, the data reveal that two well-defined attractors exist, one on each side of the separatrix. Note that the attractor located at $\eta = 0$ corresponds to the limit situation where the central pump is completely depleted and only the two lateral sidebands remain. In this case, the phase ϕ is actually illdefined, and dominant nonlinear mixing paths now become spontaneous processes. This will be characterized by the strong growth of extra sidebands, an extreme situation not taken into account in our extended model. In contrast, the attractor located at the right remains well confined within the framework of our extended theory. In Figs. 3(a) and 3(b) we display the two families of initial conditions which are attracted to the left- and right-side attractors, respectively, depending on their position on the phase-space map. The density parameter indicates how fast a given input configuration will be attracted (the lower the value is, the faster the attraction is). First, we see that attraction is much stronger for large $\Delta\xi$, but that does not change the position of the new separatrix. Notably, the new separatrix delimiting the right and left attractors differs from the ideal case. In particular, the point $\eta = 1$ now belongs exclusively to the right attractor.

With the data presented in Fig. 3, we can benchmark the performance of our model by comparing the statistical properties of trajectories computed with the segmented NLSE propagation [Figs. 3(a1) and 3(b1)] and with Eq. (6)
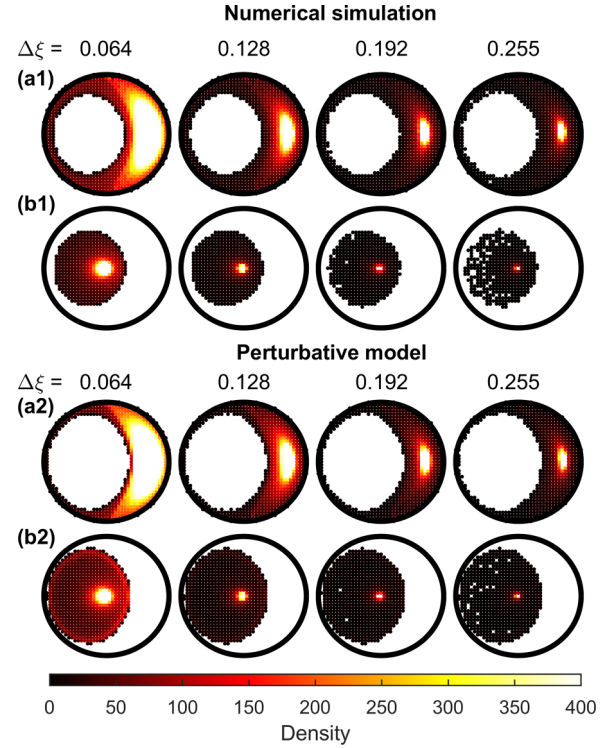

FIG. 3. Density of convergence towards (a) left- and (b) right-side stationary solutions computed by (a1) and (b1) numerically iterated NLSE propagation and (a2) and (b2) the modified FWM model at $\kappa = -2$.

[Figs. 3(a2)–3(b2)]. We see that both methods provide similar results and the dependence of the trajectories' density at different segment lengths is reproduced correctly. When the segment length is increased, the attraction region on the right side decreases, which can be explained by the more rapid change in parameters during each segment propagation so that the spiraling does not appear as gradual.

Second, we mark in Fig. 4(a) the positions of the attractors on the energy landscape defined by the system's Hamiltonian. We see that they are located in the vicinity of its extreme values: the yellow square shows the exact fixed point ($\eta_{\rm fp} = 0.7143$, $\phi_{\rm fp} = 0$) at $\kappa = -2$, while the green dot displays the
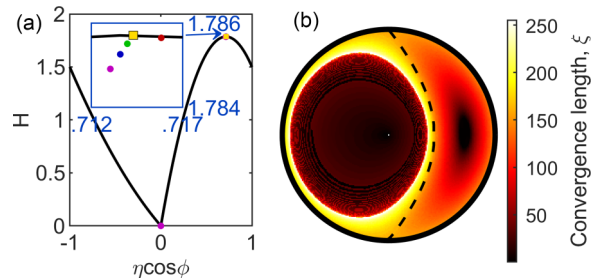

FIG. 4. (a) Attractors of the spiraling dynamics at different segment lengths $\Delta\xi$ are displayed on the Hamiltonian profile at $\kappa = -2$. The yellow square corresponds to the fixed point $\eta_{\rm fp} = 0.7143$, $\phi_{\rm fp} = 0$; red, green, blue, and magenta circles correspond to $\Delta\xi = \{0.064, 0.128, 0.192, 0.255\}$, respectively. (b) Convergence length for each initial condition on the phase-space map at $\kappa = -2$ and $\Delta\xi = 0.128$. The black dashed line indicates the separatrix position.

attractor at $\Delta\xi = 0.128$, which corresponds to the segment length that was investigated experimentally [29]. The extreme point on the left side at $\eta_{fp} = 0$ coincides perfectly with the fixed point of the ideal three-wave mixing system.

The details of the right-side attractor also confirm the importance of the stationary point. Even if the exact location differs very slightly from η_{fp}, it remains in close vicinity to the expected value. In more detail, the relative amplitude and phase values of the attractor are found to be $\eta_a = \{0.7159, 0.7143, 0.7144, 0.7144\}$ and $\phi_a = \{0.0156, 0.0312, 0.0469, 0.0625\}$ rad for $\Delta\xi = \{0.064, 0.128, 0.192, 0.255\}$, corresponding to the red, green, blue, and magenta dots in Fig. 4(a), respectively. We may, however, note a slightly more pronounced change in the relative phase of the attractor that tends to increase with the segment length.

Depending on the starting point, each trajectory converges to the attractors at a different rate; hence, different propagation distances are needed before the waves are transformed to stationary solutions. The dependence of the convergence length (defined as the length at which η is close to η_a and the relative change after two consecutive iterations is smaller than 0.01) on the position on the phase-space plane is depicted in Fig. 4(b).

We observe that the total propagation lengths required to converge to each attractor differ significantly. Trajectories on the right tend to have gradually decreasing convergence length when located closer to the attractor, while on the left side of the separatrix there is a region with short and almost homogeneous convergence lengths surrounded by a ring with much higher convergence lengths. In fact, this set of initial conditions converges not to the left but to the right-side attractor by crossing the separatrix, as depicted in Fig. 3. In other words, the convergence basins are not exclusively defined by the separatrix. As demonstrated and discussed in [30], growth of the second-order sidebands is not homogeneous on the phase-space map and is more pronounced on the right side of the separatrix. So when an initial condition corresponds to high pump energy on the left side, the contribution of the sidebands to the dynamics is minimal, so the trajectory follows the separatrix closely to a position where the second-order sidebands start to play a more significant role. Since the separatrix is an unstable solution, this small perturbation results in a change in the type of dynamics. So the trajectory can now cross the separatrix and gradually converge to the right-side attractor. This case is depicted in panels 3 of Fig. 2.

B. Dissipation and its impact on the FWM

As discussed in the previous section, the very existence of additional paths of photon interaction, represented by the higher-order harmonics, leads to deviation of the FWM dynamics from the ideal model. The developed model has shown that the second-order sidebands act as perturbations disrupting the fundamental dynamics, which leads to changes in the Hamiltonian profile. Equation (6) does not follow a pure Hamiltonian dynamical system; however, we can consider a general framework of a Hamiltonian system impaired by dissipation.

In this case, by using the definition of the conjugate variables and splitting functions responsible for the
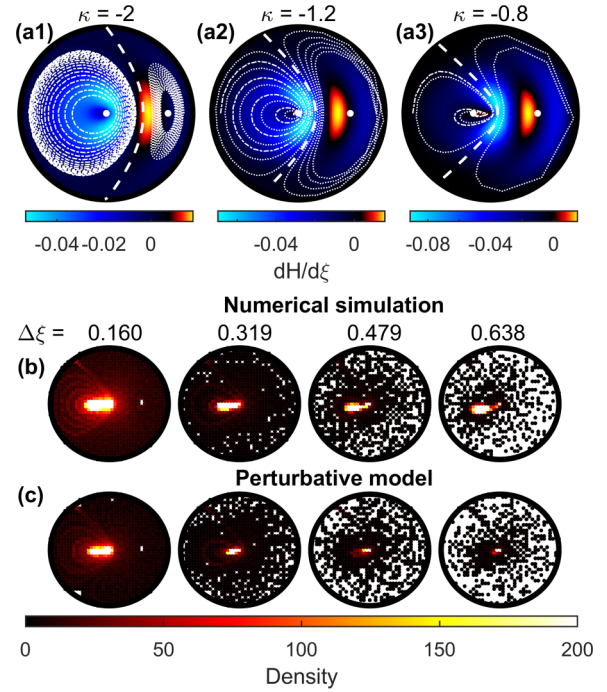

FIG. 5. (a) Distribution of the Hamiltonian dissipation according to Eq. (9) at $\Delta\xi = 0.128$. Thin white dashed and dotted lines correspond to propagation of $\eta_0 = 0.90$ and $\phi_0 = \pi$ and $\phi_0 = 0$, respectively, over $\xi = 60$. The thick white dashed line marks the position of the separatrix. White dots denote positions of stationary solutions. (b) and (c) Density of convergence towards the fixed point at $\kappa = -0.8$ and different segment lengths $\Delta\xi$.

fundamental dynamics, $\frac{d\eta}{d\xi} = \frac{dH}{d\phi} = H_\eta$ and $\frac{d\phi}{d\xi} = -\frac{dH}{d\eta} = H_\phi$, and the additional terms coming from the second-order harmonics $f_{\delta\eta, \delta\phi}$, we obtain

$$\frac{d\eta}{d\xi} = H_\eta + f_{\delta\eta}, \tag{7a}$$

$$\frac{d\phi}{d\xi} = H_\phi + f_{\delta\phi}. \tag{7b}$$

Then we take the total derivative of the Hamiltonian, which reads

$$\frac{dH}{d\xi} = \frac{\partial H}{\partial \xi} + \frac{\partial H}{\partial \eta}\frac{\partial \eta}{\partial \xi} + \frac{\partial H}{\partial \phi}\frac{\partial \phi}{\partial \xi}. \tag{8}$$

Now we can substitute the Hamiltonian derivatives by the expressions from the ideal model and the derivatives of η and ϕ by the modified expressions (7). Since the unperturbed Hamiltonian does not change during propagation $\frac{\partial H}{\partial \xi} = 0$, the dissipation of the Hamiltonian reads

$$\frac{dH}{d\xi} = H_\eta(H_\phi + f_{\delta\phi}) - H_\phi(H_\eta + f_{\delta\eta}) = H_\eta f_{\delta\phi} - H_\phi f_{\delta\eta}. \tag{9}$$

This equation represents changes in the Hamiltonian under the impact of perturbations induced by the second-order harmonics. Figure 5(a) shows the $dH/d\xi$ portrait on the phase-space map at different values of κ.

First, we observe on the left side of the separatrix that the highest decay rate is located close to $\eta = 0$, explaining the uneven spiraling rate that has been observed in this region

[dashed white line in Fig. 5(a1)]. On the right side, the decay rate is not as pronounced, and there is a region where the Hamiltonian is actually recovering ($dH/d\xi$ positive), which further slows down the global spiraling that is observed in this region.

Second, in Figs. 5(a1)–5(a3), we see that the loci of regions with growth or decay are more or less preserved and do not depend much on either $\Delta\xi$ or the value of the nonlinearity κ. This implies that the dissipation mechanism depends mainly on the relation between the phases and amplitudes of the pump and the sidebands but not on the type of dynamics (i.e., with bounded and unbounded phases on the right and left sides of the separatrix, respectively). With the growth of κ (e.g., with higher nonlinearity), we observe that dissipation and changes in the Hamiltonian become more significant. Consequently, the nominal ideal dynamics can be modified significantly enough during a single segment of propagation $\Delta\xi$ that it crosses the separatrix [dotted white lines in Figs. 5(a2) and 5(a3)]. The existence of localized regions with high losses also explains the rapid spiraling on the left side after just a half orbit.

To verify the statistical properties of the systems with higher nonlinearity, for instance, $\kappa = -0.8$, we performed a few simulations similar to those in Fig. 4. The results are presented in Figs. 5(b) and 5(c) for numerical simulation and our modified model, respectively. We observe that the system converges only to the fixed point $\eta_{\mathrm{fp}} = 0$ on the left side of the separatrix for any segment length. Even trajectories passing close to the right-side fixed point ($\eta_{\mathrm{fp}} = 0.543$, $\phi_{\mathrm{fp}} = 0$) converge to the left side. This behavior denotes a complete change in the dynamics (transition from two stable fixed points to only one).

Third, we can now justify why the system is spiraling to the fixed points. From the distributions presented in Fig. 5(a), we see that the fixed points (marked as white dots) are located at zero-dissipation values and extremes of the Hamiltonian energy. On the left side, the dissipation has a negative value, and the fixed point is a minimum of the energy, hence forming a stable attractor [as in Figs. 5(a1) and 5(a2)]. In contrast, on the right side of the separatrix, the fixed point is located between the growth and decay regions, hence forming a saddle point. Therefore, this fixed point gradually becomes more and more unstable as the nonlinearity (i.e., $1/|\kappa|$) is increased [as in Fig. 5(a3)].

V. DISCUSSION

In previous works, the differences between the evolution of the idealized FWM model and the of a real fiber system were attributed to gradual depletion of energy located inside the three central harmonics, which is linked to the cascade of the FWM events. In the present work, we can trace the origin of the observed divergences to the very existence of the second-order harmonics, which allows additional nonlinear mixing possibilities. While they carry little energy, the resulting dynamics may differ significantly from the ideal model.

This study bridges the gap between the ideal system, in which only three spectral lines participate in the dynamics [12,14], and the full-spectrum wave mixing during the MI dynamics [39]. The modified model Eq. (6) provides a quantitative description of the cumulative impact of the higher-order sidebands. It could be relevant for systems undergoing parametric wave mixing [35,38] and for explaining spontaneous FPUT recurrence breaking in optical fibers. Furthermore, we discussed a method to include the higher-order sidebands in intrinsically three-wave dynamics, which could help us to describe the spatial Benjamin-Feir instability where the second-order harmonics are linearly stable [40].

On the left side of the separatrix (or on both sides in the case of high nonlinearity), we observe a full conversion of the pump power to the sidebands at any initial condition. This allows the potential implementation of the gain through losses mechanism [41] in our experimental configuration. Indeed, it has been demonstrated that by introducing wavelength-dependent distributed losses [42] or a chain of filters [41], one can induce an optical gain that results in a new type of MI [43] or more efficient signal amplification during the FWM process [44]. This type of instability is different from the parametric gain occurring at special resonant conditions under the effects of periodic variation of power [45] or dispersion [46–48].

VI. CONCLUSION

In the present work, we demonstrated that the very existence of photon-exchange paths with higher-order harmonics can lead to the disturbance of the fundamental FWM dynamics. We investigated the nonconservation of the truncated FWM dynamics under a perturbative impact of the second-order sidebands. We developed a modified model in terms of canonical pairs of Hamiltonian variables in which some additional photon interaction paths are included, which allows a more precise description of the experimental dynamics observed in [29,30]. The discussion of the dissipation mechanisms impairing the nominal Hamiltonian dynamics allowed us to unveil the origin of this peculiar dynamics that is observed experimentally. The spiraling behavior of the trajectories is, in particular, now fully explained. We demonstrated especially that the impact of the second-order harmonics can actually be considered a perturbation, which leads to the appearance of coherent dissipation of either the positive or negative sign. This approach could, in principle, be generalized to any system subject to perturbations.

Similar to nonlinear fiber optics, deepwater wave propagation in hydrodynamics can be described by the NLSE, so we can make a link between dissipation in these systems. Waves propagating in a water tank are impaired by friction and viscosity, which impacts the FPUT recurrence [49] and can lead to a change in the dynamics type. In deepwater approximations, the perturbations can be caused by the effects of damping and forcing [50], which ultimately leads to the crossing of the separatrix, and by a change in the dynamics [20,28]. In our case, even though the dissipation has a different nature, it can still be considered a finite (namely, three-wave) system impaired by an external dissipation process, which is here in the form of an exchange of energy with higher-order harmonics. Therefore, such an approach can be applied to other dynamics, which allows us to achieve a more accurate description while retaining a simple analytical model.

Our approach relies on adiabatic elimination by assuming a constant phase and an average spectral amplitude of the

second-order harmonics over each fiber segment, which, on the one hand, allows a simple analytical formulation of the modified equation but, on the other hand, is valid only for a short segment of fiber. A complementary approach for the case of a longer fiber segment would be to identify the relevant distributed model by means of data-driven techniques aiming to identify nonlinear dynamics [51].

This work can also be used to gain an understanding and develop new types of fiber-optic parametric amplifiers. Indeed, filtering out the second-order harmonics at each iteration allows conversion between states that are not located on the same trajectory. Our work, which encompasses a complete study of how the dynamics is affected by different initial conditions and introduces the Hamiltonian analysis, could improve the understanding of how such systems are affected by asymmetric losses.

APPENDIX: COMPLETE SET OF EQUATIONS FOR SPECTRAL PHASES AND AMPLITUDES

In order to define the cumulative effect of the second-order sidebands, we include the extra processes that involve generation of the respective spectral lines. Assuming a small level of nonlinearity ($\kappa < -1$), we can include only photon-exchange paths that involve the central lines and one of the sidebands, as depicted in Fig. 6.

Considering only symmetric evolution (hence, the asymmetry invariant equals zero [12,30]), which implies equal
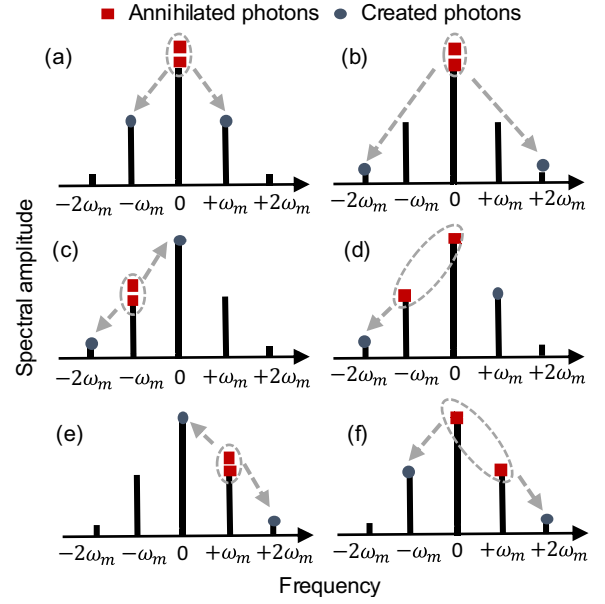

FIG. 6. [(a)–(f)] Possible processes of energy exchange between the three central lines and the second-order sidebands. In (a) the nominal three-wave formulation allows only one mixing process. All the other processes indeed imply the transfer of energy to either the $+2$ or -2 sideband. In (b) the spontaneous breaking of a pair of pump photons into both $+2$ and -2 sidebands is negligible in comparison to the others processes in (a) and (c)–(f), which are the stimulated ones.

changes in phase and amplitude of the $+n\omega_m$ and $-n\omega_m$ spectral lines, we can denote spectral amplitudes and phases as $a_{-n} = a_{+n} = a_{\pm n}$ and $\varphi_{-n} = \varphi_{+n} = \varphi_{\pm n}$ ($n = 1, 2$), respectively. Then the coupled equations presented in [12] are modified as follows:

$$\frac{da_0}{d\xi} = -2a_{\pm 1}^2 a_0 \sin(2\varphi_{\pm 1} - 2\varphi_0) - 4a_{\pm 2}a_{\pm 1}^2 \sin(\varphi_{\pm 2} - \varphi_0) - 2a_{\pm 1}^2 a_{\pm 2} \sin(2\varphi_{\pm 1} - \varphi_{\pm 2} - \varphi_0),$$

$$\frac{da_{\pm 1}}{d\xi} = -a_0^2 a_{\pm 1} \sin(2\varphi_0 - 2\varphi_{\pm 1}) - 2a_{\pm 2}a_{\pm 1}a_0 \sin(\varphi_{\pm 2} + \varphi_0 - 2\varphi_{\pm 1}),$$

$$\frac{da_{\pm 2}}{d\xi} = -a_{\pm 1}^2 a_0 \sin(2\varphi_{\pm 1} - \varphi_0 - \varphi_{\pm 2}) - 2a_0 a_{\pm 1}^2 \sin(\varphi_0 - \varphi_{\pm 2}), \tag{A1}$$

$$\frac{d\varphi_0}{d\xi} = a_0^2 + 4a_{\pm 1}^2 + 4a_{\pm 2}^2 + 2a_{\pm 1}^2 \cos\phi + \frac{4a_{\pm 2}a_{\pm 1}^2}{a_0}\cos(\varphi_{\pm 2} - \varphi_0) + \frac{a_{\pm 2}a_{\pm 1}^2}{a_0}\cos(\varphi_{\pm 2} + \varphi_0 - 2\varphi_{\pm 1}),$$

$$\frac{d\varphi_{\pm 1}}{d\xi} = \frac{1}{2}\kappa + 2a_0^2 + 3a_{\pm 1}^2 + 4a_{\pm 2}^2 + a_0^2\cos\phi + 4a_0 a_{\pm 2}\cos(\varphi_{\pm 2} - \varphi_0) + 2a_0 a_{\pm 2}\cos(\varphi_{\pm 2} + \varphi_0 - 2\varphi_{\pm 1}),$$

$$\frac{d\varphi_{\pm 2}}{d\xi} = 2\kappa + 2a_0^2 + 4a_{\pm 1}^2 + 3a_{\pm 2}^2 + \frac{a_{\pm 1}^2 a_0}{a_{\pm 2}}\cos(\varphi_{\pm 2} + \varphi_0 - 2\varphi_{\pm 1}) + \frac{2a_{\pm 1}^2 a_0}{a_{\pm 2}}\cos(\varphi_{\pm 2} + \varphi_0). \tag{A2}$$

Since the energy of three lines is conserved in the first approximation and the accumulated energy in the second-order sidebands remains small, we can denote $a_{\pm 1} = \sqrt{(1 - \eta)/2}$. Substituting this simplification in Eqs. (A1) and (A2) and using the definition

$a_0 = \sqrt{\eta}$ result in

$$\frac{da_0}{d\xi} = -(1-\eta)\sqrt{\eta}\sin(2\varphi_{\pm1} - 2\varphi_0) - 2a_{\pm2}(1-\eta)\sin(\varphi_{\pm2} - \varphi_0) - (1-\eta)a_{\pm2}\sin(2\varphi_{\pm1} - \varphi_{\pm2} - \varphi_0),$$

$$\frac{da_{\pm1}}{d\xi} = -\eta\sqrt{(1-\eta)/2}\sin(2\varphi_0 - 2\varphi_{\pm1}) - a_{\pm2}\sqrt{2(1-\eta)}\sqrt{\eta}\sin(\varphi_{\pm2} + \varphi_0 - 2\varphi_{\pm1}),$$

$$\frac{da_{\pm2}}{d\xi} = -(1-\eta)/2\sqrt{\eta}\sin(2\varphi_{\pm1} - \varphi_0 - \varphi_{\pm2}) - \sqrt{\eta}(1-\eta)\sin(\varphi_0 - \varphi_{\pm2}), \tag{A3}$$

$$\frac{d\varphi_0}{d\xi} = 2 - \eta + 4a_{\pm2}^2 + (1-\eta)\cos\phi + \frac{2a_{\pm2}(1-\eta)}{\sqrt{\eta}}\cos(\varphi_{\pm2} - \varphi_0) + \frac{a_{\pm2}(1-\eta)}{2\sqrt{\eta}}\cos(\varphi_{\pm2} + \varphi_0 - 2\varphi_{\pm1}),$$

$$\frac{d\varphi_{\pm1}}{d\xi} = \frac{1}{2}\kappa + 2\eta + 3(1-\eta)/2 + 4a_{\pm2}^2 + \eta\cos\phi + 4\sqrt{\eta}a_{\pm2}\cos(\varphi_{\pm2} - \varphi_0) + 2\sqrt{\eta}a_{\pm2}\cos(\varphi_{\pm2} + \varphi_0 - 2\varphi_{\pm1}),$$

$$\frac{d\varphi_{\pm2}}{d\xi} = 2\kappa + 2\eta + 2(1-\eta) + 3a_{\pm2}^2 + \frac{(1-\eta)\sqrt{\eta}}{2a_{\pm2}}\cos(\varphi_{\pm2} + \varphi_0 - 2\varphi_{\pm1}) + \frac{(1-\eta)\sqrt{\eta}}{a_{\pm2}}\cos(\varphi_{\pm2} + \varphi_0). \tag{A4}$$

Integrating Eq. (A3) over a short segment of fiber $\Delta\xi$ results in Eq. (4). The stationary phase condition for the second-order harmonics $\frac{d\varphi_{\pm2}}{d\xi} = 0$ applied to Eq. (A4) results in Eq. (5).

[1] G. P. Agrawal, *Nonlinear Fiber Optics*, 6th ed. (Academic Press, San Francisco, CA, 2019).

[2] B. Kibler, A. Chabchoub, A. Gelash, N. Akhmediev, and V. E. Zakharov, Phys. Rev. X **5**, 041026 (2015).

[3] P. Jha, P. Kumar, G. Raj, and A. K. Upadhyaya, Phys. Plasmas **12**, 123104 (2005).

[4] V. Zakharov and L. Ostrovsky, Phys. D (Amsterdam, Neth.) **238**, 540 (2009).

[5] A. Barthelemy and R. De La Fuente, Opt. Commun. **73**, 409 (1989).

[6] F. Copie, S. Randoux, and P. Suret, Rev. Phys. **5**, 100037 (2020).

[7] A. Hasegawa, Opt. Lett. **9**, 288 (1984).

[8] K. Hammani, B. Wetzel, B. Kibler, J. Fatome, C. Finot, G. Millot, N. Akhmediev, and J. M. Dudley, Opt. Lett. **36**, 2140 (2011).

[9] J. R. Thompson and R. Roy, Phys. Rev. A **44**, 7605 (1991).

[10] D. L. Hart, A. Judy, T. A. Brian Kennedy, R. Roy, and K. Stoev, Phys. Rev. A **50**, 1807 (1994).

[11] X. Liu, X. Zhou, and C. Lu, Phys. Rev. A **72**, 013811 (2005).

[12] G. Cappellini and S. Trillo, J. Opt. Soc. Am. B **8**, 824 (1991).

[13] S. Trillo, S. Wabnitz, and T. A. B. Kennedy, Phys. Rev. A **50**, 1732 (1994).

[14] S. Trillo and S. Wabnitz, Opt. Lett. **16**, 986 (1991).

[15] E. Fermi, P. Pasta, S. Ulam, and M. Tsingou, Los Alamos National Laboratory Technical Report, 1955.

[16] N. N. Akhmediev, Nature (London) **413**, 267 (2001).

[17] M. Onorato, L. Vozella, D. Proment, and Y. V. Lvov, Proc. Natl. Acad. Sci. USA **112**, 4208 (2015).

[18] A. Mussot, A. Kudlinski, M. Droques, P. Szriftgiser, and N. Akhmediev, Phys. Rev. X **4**, 011054 (2014).

[19] G. Vanderhaegen, P. Szriftgiser, A. Kudlinski, M. Conforti, A. Armaroli, and A. Mussot, Phys. Rev. A **106**, 033519 (2022).

[20] D. Eeltink, A. Armaroli, C. Luneau, H. Branger, M. Brunetti, and J. Kasparian, Nonlinear Dyn. **102**, 2385 (2020).

[21] X. Wang, Z. Dong, and Z. Deng, Results Phys. **29**, 104715 (2021).

[22] G. Vanderhaegen, P. Szriftgiser, A. Kudlinski, M. Conforti, S. Trillo, M. Droques, and A. Mussot, Opt. Express **28**, 17773 (2020).

[23] C. Naveau, G. Vanderhaegen, P. Szriftgiser, G. Martinelli, M. Droques, A. Kudlinski, M. Conforti, S. Trillo, N. Akhmediev, and A. Mussot, Front. Phys. **9**, 637812 (2021).

[24] X. Hu, W. Chen, Y. Lu, Z. Yu, M. Chen, and Z. Meng, IEEE Photonics Technol. Lett. **30**, 47 (2018).

[25] G. Xu, A. Chabchoub, D. E. Pelinovsky, and B. Kibler, Phys. Rev. Res. **2**, 033528 (2020).

[26] C. Naveau, P. Szriftgiser, A. Kudlinski, M. Conforti, S. Trillo, and A. Mussot, Opt. Lett. **44**, 763 (2019).

[27] G. Xu, K. Hammani, A. Chabchoub, J. M. Dudley, B. Kibler, and C. Finot, Phys. Rev. E **99**, 012207 (2019).

[28] A. Armaroli, D. Eeltink, M. Brunetti, and J. Kasparian, Phys. Fluids **30**, 017102 (2018).

[29] A. Sheveleva, U. Andral, B. Kibler, P. Colman, J. M. Dudley, and C. Finot, Optica **9**, 656 (2022).

[30] A. Sheveleva, P. Colman, J. M. Dudley, and C. Finot, Ann. Phys. (Berlin, Ger.) **536**, 2300489 (2024).

[31] M. E. Marhic, P. A. Andrekson, P. Petropoulos, S. Radic, C. Peucheret, and M. Jazayerifar, Laser Photonics Rev. **9**, 50 (2015).

[32] S. Trillo and S. Wabnitz, Opt. Lett. **16**, 1566 (1991).

[33] A. Sheveleva, P. Colman, J. M. Dudley, and C. Finot, Opt. Commun. **538**, 129472 (2023).

[34] C. Naveau, P. Szriftgiser, A. Kudlinski, M. Conforti, S. Trillo, and A. Mussot, Opt. Lett. **44**, 5426 (2019).

[35] Y. Chen and A. W. Snyder, Opt. Lett. **14**, 87 (1989).

[36] A. Vatarescu, J. Lightwave Technol. **5**, 1652 (1987).

[37] M. Marhic, *Fiber Optical Parametric Amplifiers, Oscillators and Related Devices* (Cambridge University Press, Cambridge, 2008).

[38] J. Hansryd, P. Andrekson, M. Westlund, J. Li, and P.-O. Hedekvist, IEEE J. Sel. Top. Quantum Electron. **8**, 506 (2002).

[39] M. Conforti, A. Mussot, A. Kudlinski, S. Trillo, and N. Akhmediev, Phys. Rev. A **101**, 023843 (2020).

[40] C. Heffernan, A. Chabchoub, and R. Stuhlmeier, Wave Motion **130**, 103381 (2024).

[41] A. M. Perego, S. K. Turitsyn, and K. Staliunas, Light: Sci. Appl. **7**, 43 (2018).

[42] K. Xu, H. Liu, Y. Dai, J. Wu, and J. Lin, Opt. Commun. **285**, 790 (2012).

[43] T. Tanemura, Y. Ozeki, and K. Kikuchi, Phys. Rev. Lett. **93**, 163902 (2004).

[44] C. Jauregui, A. Steinmetz, J. Limpert, and A. Tünnermann, Opt. Express **20**, 24957 (2012).

[45] F. Matera, A. Mecozzi, M. Romagnoli, and M. Settembre, Opt. Lett. **18**, 1499 (1993).

[46] M. Conforti, A. Mussot, A. Kudlinski, S. Rota Nodari, G. Dujardin, S. De Biévre, A. Armaroli, and S. Trillo, Phys. Rev. Lett. **117**, 013901 (2016).

[47] N. J. Smith and N. J. Doran, Opt. Lett. **21**, 570 (1996).

[48] J. C. Bronski and J. N. Kutz, Opt. Lett. **21**, 937 (1996).

[49] O. Kimmoun, H. C. Hsu, H. Branger, M. S. Li, Y. Y. Chen, C. Kharif, M. Onorato, E. J. R. Kelleher, B. Kibler, N. Akhmediev, and A. Chabchoub, Sci. Rep. **6**, 28516 (2016).

[50] C. Kharif, R. A. Kraenkel, M. A. Manna, and R. Thomas, J. Fluid Mech. **664**, 138 (2010).

[51] A. V. Ermolaev, A. Sheveleva, G. Genty, C. Finot, and J. M. Dudley, Sci. Rep. **12**, 12711 (2022).